Journal of The Electrochemical Society, **150** (9) E429-E437 (2003)
0013-4651/2003/150(9)/E429/9/$7.00 © The Electrochemical Society, Inc.

EIS Studies of Porous Oxygen Electrodes with Discrete Particles

II. Transmission Line Modeling

Chad C. Waraksa,[a] Guoying Chen,[a] Digby D. Macdonald,[b,*,z] and Thomas E. Mallouk[a,]**

[a]*Department of Chemistry and* [b]*Department of Materials Science and Engineering, The Pennsylvania State University, University Park, Pennsylvania 16802, USA*

Porous electrodes provide high-surface-area supports for the catalysts of many reactions, but the influences of electrode preparation conditions on electrocatalysts are not always well understood. Electrochemical impedance spectroscopy (EIS) can provide extensive information about an electrode, but the models describing the spectra are often too idealized to draw useful conclusions. We describe a new model based on an array of parallel, nonuniform transmission lines for predicting the response of porous electrodes. The model incorporates physically realistic elements, such as discrete particles of variable size and adjustable multilayer stacking geometries. Resistance parameters were derived from experimental data for Pt_4Ru_4Ir-coated $Ti_{0.9}Nb_{0.1}O_2$ and Ebonex electrodes prepared under varying degrees of oxidative conditioning. The results, which indicate a high degree of impedance at the support-solution interface and consequently, low catalyst utilization, suggest several strategies for improved electrode design.
 [DOI: 10.1149/1.1594730]

Manuscript submitted July 12, 2002; revised manuscript received March 6, 2003. Available electronically July 15, 2003.

Porous electrodes are important in electrochemical systems because they can dramatically increase the active surface area available for reactions and provide ideal supports for finely divided noble-metal catalysts. Unfortunately, properties of such systems are often incompletely understood, as small, high-surface-area particles may not behave as they would in bulk phase. Electrochemical impedance spectroscopy (EIS) is a technique that in principle provides detailed information about a multicomponent electrode, but the interpretation of impedance spectra for porous electrodes is difficult. Among other applications, impedance spectroscopy has been used to study chloride oxidation on electrodes[1] and the capacitance of nickel electrodes.[2] Simple equivalent circuit,[3] finite element,[4] and transmission line models have been used to analyze spectra of electrodes assuming conical[5] or uniformly cylindrical[6] pores and spectra of individual pores of various shapes have been calculated,[7] but all of these systems are highly idealized.

We have recently synthesized and characterized a catalyst useful for both the oxidation of water and the reduction of oxygen in regenerative fuel cells.[8] These materials consist of Pt_4Ru_4Ir metals and corresponding metal oxides coating spheroidal support particles comprising either $Ti_{0.9}Nb_{0.1}O_2$ or the TiO_2 suboxide material Ebonex (Ti_nO_{2n-1},$4 \leq n \leq 10$). These electrodes exhibit different stabilities under oxygen-rich environments at high temperatures or high anodic potentials. It has been hypothesized that the performance deterioration after oxidative conditioning arises from oxidation of the support, which increases its resistivity. In order to extract particle resistivities from EIS data, we have constructed what we believe to be the first porous electrode transmission line model that incorporates such physically realistic features as discrete support particles of variable diameter and adjustable thickness and separation geometries.

Experimental

Porous electrodes were prepared by coating Toray carbon paper disks with supported catalyst inks, as described in detail elsewhere.[9,10] The approximate coverage fraction was determined by examining a scanning electron microscope (SEM) image of the electrode surface collected using a JEOL-JSM 5400 microscope at the Electron Microscope Facility at The Pennsylvania State University. This coverage value was used for comparison, but not as part of the model. The particle size distribution was obtained using the Princeton Gamma Technologies IMIX program and was incorporated into the surface model.

Modeling the Electrode Surface Geometry

The carbon electrode surface was modeled as a plane covered with one or more hexagonally arranged layers of conducting spheres surrounded by a sulfuric acid electrolyte solution. Analysis of SEM micrographs of an electrode[10] indicated that the sphere diameters D (μm) obeyed a lognormal distribution with $\mu = 1.24(2)$ and $\sigma = 0.28(2)$ for a 494 particle sample whose probability density function is given by

$$P[D] = \frac{e^{-1/2(\ln[D]-\mu/\sigma)^2}}{D\sigma\sqrt{2\pi}} \quad [1]$$

The density ρ of the support particles was known to be 4.15 g/cm^3, and the total mass m deposited on the electrode surface was 2 mg. This enabled calculation of the number of particles N_{part} coating the surface as

$$N_{\text{part}} = \frac{m}{\rho\frac{4}{3}\pi\langle r^3\rangle} \quad [2]$$

$$N_{\text{part}} = \frac{6m}{\pi\rho\int_0^\infty D^3 p[D]dD} \quad [3]$$

This was determined to be approximately 1.59×10^7 spheres spread out unevenly over an area of 2.45 cm^2. SEM images indicated that an estimated 85% of the surface was covered with spheres, representing an effective area of 2.1 cm^2.

For simplicity the model initially chose to ignore the disorder observed in the electrode surface and to assume a single layer of spheres located within a minimally large hexagonal ''unit cell'' whose size varied with the particle radius. The model required no assumptions as to whether individual spheres or unit cells touched one another (close packing) or were isolated in islands. Despite its simplicity, this model indicated 1.59×10^7 spheres produce a surface coverage of 1.9 cm^2, within 9% of the observed value.

* Electrochemical Society Fellow.
** Electrochemical Society Active Member.
z E-mail: ddm2@psu.edu

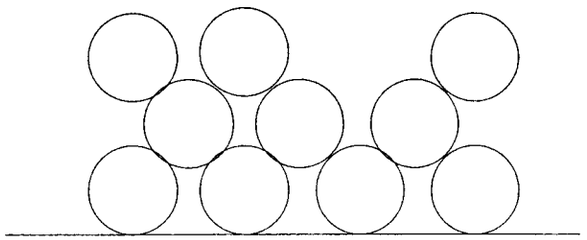

Figure 1. Representation of fractional layers.

Unfortunately, this model was insufficient to generate impedance spectroscopy loci consistent with those experimentally observed.

To resolve this, a multilayer surface model was developed. It was assumed that a surface possessing the average number of layers, n_{avg}, was composed of two integer numbers of sphere layers n_{base} (the integer portion of n_{avg}) and $n_{base} + 1$, as shown in Fig. 1. The coverage n_{frac} of the thicker region was taken as the noninteger portion of n_{avg} and the coverage of the thinner layer was $1 - n_{frac}$. Spheres of radius r were assumed to be hexagonally arranged but not necessarily close packed. Sphere-sphere separations X on the base layer were described as $X = fr$ where f is a dimensionless separation factor varying between 2 (close packed) and $2\sqrt{3}$ (where close packing resumes because of interpenetration of the supported layers). In multilayer regions, each sphere not in the uppermost layer was assumed to be in contact with three spheres resting atop it, with every other layer centered on alternating corners of the hexagonal unit cell, as seen in Fig. 2. As a concession to mathematical practicality, these spheres were made of the same diameter as the base sphere. As mathematically idealized spheres, multilayers had only tangential points of contact with one another; any resulting interactions were neglected.

Transmission Line Models

It has been shown[11] that porous electrochemically active surfaces can be effectively simulated using transmission line models. Such models divide a surface into numerous vertically stacked segments, each possessing its own impedances due to the presence of electrolyte solution R_s, the conducting or semiconducting support material R_m, and an interfacial impedance Z.

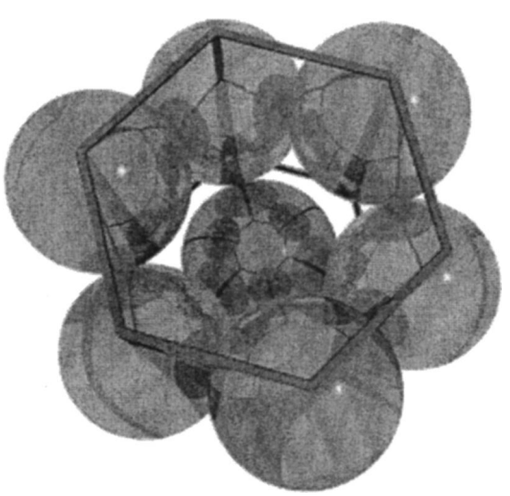

Figure 2. Top-down view of multilayer unit cell.

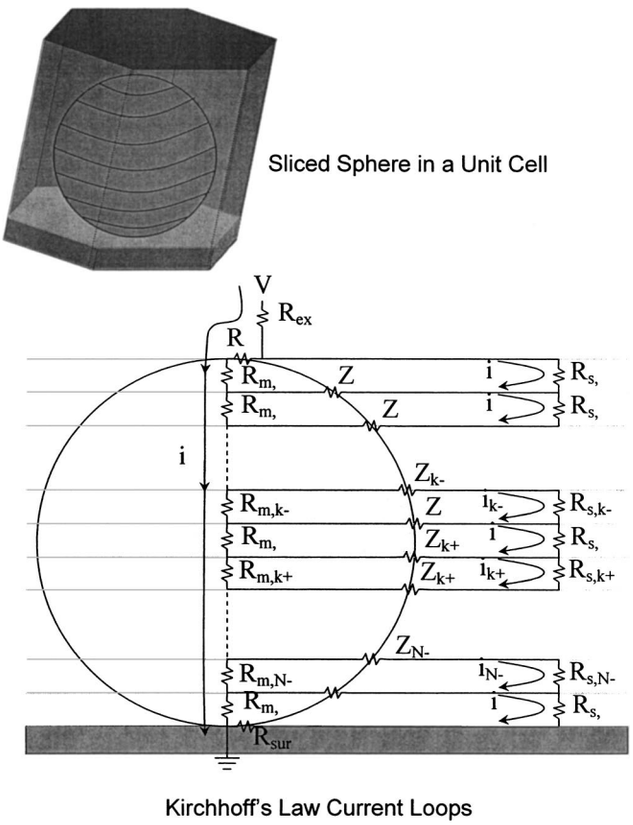

Figure 3. Segmentation of unit cell into current loops.

After passing through an external resistance to reach the outermost part of the electrode surface, current may either continue to pass through slices of the electrolyte solution or may pass through an interface and continue through the particle. As shown in Fig. 3, Kirchhoff's voltage law may be applied both to the entire unit cell

$$i_0\left(R_{ext} + Z_1 + \sum_{k=1}^{N} R_{m,k}\right) - i_1 Z_1 - \sum_{k=1}^{N} i_k R_{m,k} = V$$

$$i_0 R_{ext} + \sum_{k=1}^{N} i_k R_{s,k} + i_N Z_{surf} = V \quad [4]$$

and to each of the N segments

$$-i_0(Z_1 + R_{m,1}) + i_1(Z_1 + R_{s,1} + Z_2 + R_{m,1}) - i_2 Z_2 = 0 \quad [5]$$

$$-i_0 R_{m,k} - i_{k-1} Z_k + i_k(Z_k + R_{s,k} + Z_{k+1} + R_{m,k}) - i_{k+1} Z_{k+1} = 0 \quad [6]$$

$$k = 2...N - 1$$

$$-i_0 R_{m,N} - i_{N-1} Z_N + i_N(Z_N + R_{s,k} + Z_{surf} + R_{m,k}) = 0 \quad [7]$$

This system of equations allows us to solve[12,c] for the unit cell impedance Z_{cell}

[c] Tridiagonal matrix and nonlinear optimization routines were based upon those found in Ref. 12.

$$Z_{cell} = R_{ext} + \sum_{k=1}^{N} (1 - X_k)R_{m,k} + (1 - X_1)Z_1 = R_{ext} + \sum_{k=1}^{N} X_k R_{s,k} + X_N Z_{surf} \quad [8]$$

which is evaluated using the rightmost expression to minimize the number of operations on complex numbers. These unit cell impedances depend upon the diameter of the enclosed spheres. The porous electrode impedance Z_{PE} is calculated from these parallel cell impedances and is weighted for their frequency of occurrence

$$\frac{1}{Z_{PE}} = \sum^{\text{all radii}} \frac{(Number\ of\ spheres\ on\ surface)*p[D]}{Z_{cell}[D]} \quad [9]$$

The number of spheres touching the surface (with their own unit cell) is simply the total number of spheres over the number of layers times the fraction of the surface with that number of layers. Z_{PE} is calculated in this manner for each frequency of interest and compared with the experimental value. This model used 50 radii evenly spaced between the minimum and maximum observed radii and those frequencies actually collected during the impedance spectroscopy experiments.

The model contained one fixed parameter, the known[13] resistivity of the electrolyte solution $\rho_s = 4.46\ \Omega$ cm and set the number of particles and their size distribution based upon experimental observation. Fits were based on eight adjustable parameters: the resistivity of the spherical material on the surface ρ_m (Ω cm), the *RC* time constants of the particle wall-solution interface and the electrode surface interface RC_w and RC_s(s), the specific resistances of the particle wall and electrode surface, R_w and R_{surf} (Ω cm^2), the external cell specific resistance R_{ext} (Ω cm^2), the number of layers n_{avg}, and the separation factor *f*. N_{avg} was required to be at least one, the separation factor was held within the limits discussed, and all other parameters were constrained to positive values.

The model contained no explicit representation of the Pt_4Ru_4Ir catalyst (or any possible oxidation products) contained on the support surface. Although these materials likely constitute discrete particles on the spheroidal supports, they were assumed to be uniformly distributed across the surface, and their influences to be incorporated into the R_w and RC_w terms. It was also assumed that no current flowed into the carbon paper support except at the contact point between the support material sphere and the electrode surface and that this interface had a contact area equal to the surface area of the final slice of the base sphere.

Division of Transmission Line Segments

To take advantage of vertical symmetry, each multilayered unit cell was conceptually divided into three distinct repeating regions. Symmetry here refers to that of electrochemically important elements, such as impedances and the cross-sectional and surface areas from which they are calculated; the physical locations of particles are often displaced horizontally within a slice. Wherever symmetry was found, impedance calculations were performed only on the asymmetric regions.

Although the stacking geometry varies depending upon the value of *f*, these regions are named based on the case of relatively tight packing, as shown in Fig. 4. The first region at the base and top of the stack begins with a single sphere and continues until meeting another sphere. This is dubbed the incremental height (IH) region, because its thickness is the net height increase with each succeeding layer of spheres. There are always exactly two of these regions. The second zone, the overlap band (OB), contains multiple spheres in each slice and may repeat several times throughout the unit cell. The third region, the interlayer gap (G), occurs between overlap bands and is named for the tightly packed case where there is a gap between the onset of the first and third layers.

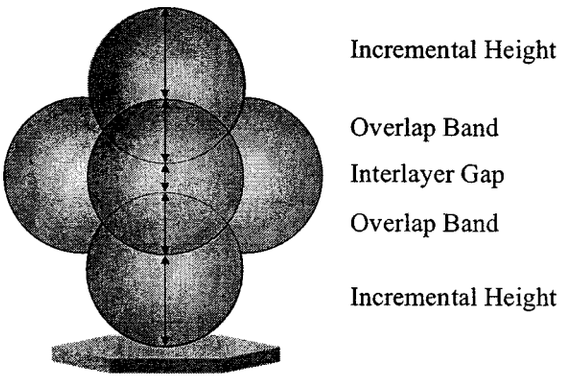

Figure 4. Slicing a multilayer unit cell.

The stacking geometry, however, determines the actual contents of these regions. In tightly packed cases where $2 \leq f \leq 3$, the incremental height exceeds one radius, so there is always a gap between the first and third layers. These unit cells, typified by Fig. 5a, always possess an incremental height region at their top and base, followed by alternating overlap bands containing two spheres and gap regions intersecting only a single sphere per slice. This describes the system found on our electrodes.

On surfaces such as that shown in Fig. 5b, $3 < f < 4\sqrt{2/3}$ and the incremental height is less than one radius length, causing the third layer of spheres to begin before the first is completed. In these situations, the IH region is expanded to include the initial portion of the second layer. The overlap band then contains three spheres before becoming the gap region possessing only two spheres. As *f* increases, this gap narrows and the layers become progressively thinner.

In the final case, $4\sqrt{2/3} \leq f < 2\sqrt{3}$, depicted in Fig. 5c, the gap has narrowed until the fourth layer now rests atop the first and cannot sink further. In these cases, both the overlap band and the interlayer gap (which now intersects other layers) contain three spheres but are preserved as distinct regions for convenient divisions at sphere boundaries. Unlike the first two cases, the top and base overlap bands (containing first one and then two spheres) are not symmetric unless the number of layers is a multiple of three. Asymmetry arises when the top one or two layers sit directly atop the underlying sphere rather than obtaining support from the three spheres in the previous layer. In these situations, necessity dictates two distinct sets of calculations for the IH region. It is also worth noting that if *f* ever reaches $2\sqrt{3}$, three layers collapse into a single closely packed layer and *f* returns to 2. Indeed, the simulated spectra for a six-layer system with high *f* is very similar to that for an otherwise identical close-packed two-layer system

Because the program used to fit the impedance data prespecifies a total (even) number of symmetric slices, the number of slices falling within each region can vary widely depending upon the number of layers. Moreover, regions delineating the sphere boundaries needed for proper calculations often require slice thicknesses to vary slightly from zone to zone. Hence, the number of slices in each zone is first calculated, rounded to an integer, and then used to calculate the segment thickness. For generality, calculations are performed using dimensionless radius units of total thickness *T*, separation factor *f*, and the number of layers *n*, and the total number of slices *N*/2 in one asymmetric half of the cell. Values are calculated for each slice in the asymmetric IH region, and for the asymmetric halves of the OB and G regions, containing n_{IH}, n_{OB}, and n_G slices and having thicknesses of *IH*, *OB*, and *G*, respectively.

For geometries where $f < 4\sqrt{2/3}$, the total thickness *T* is

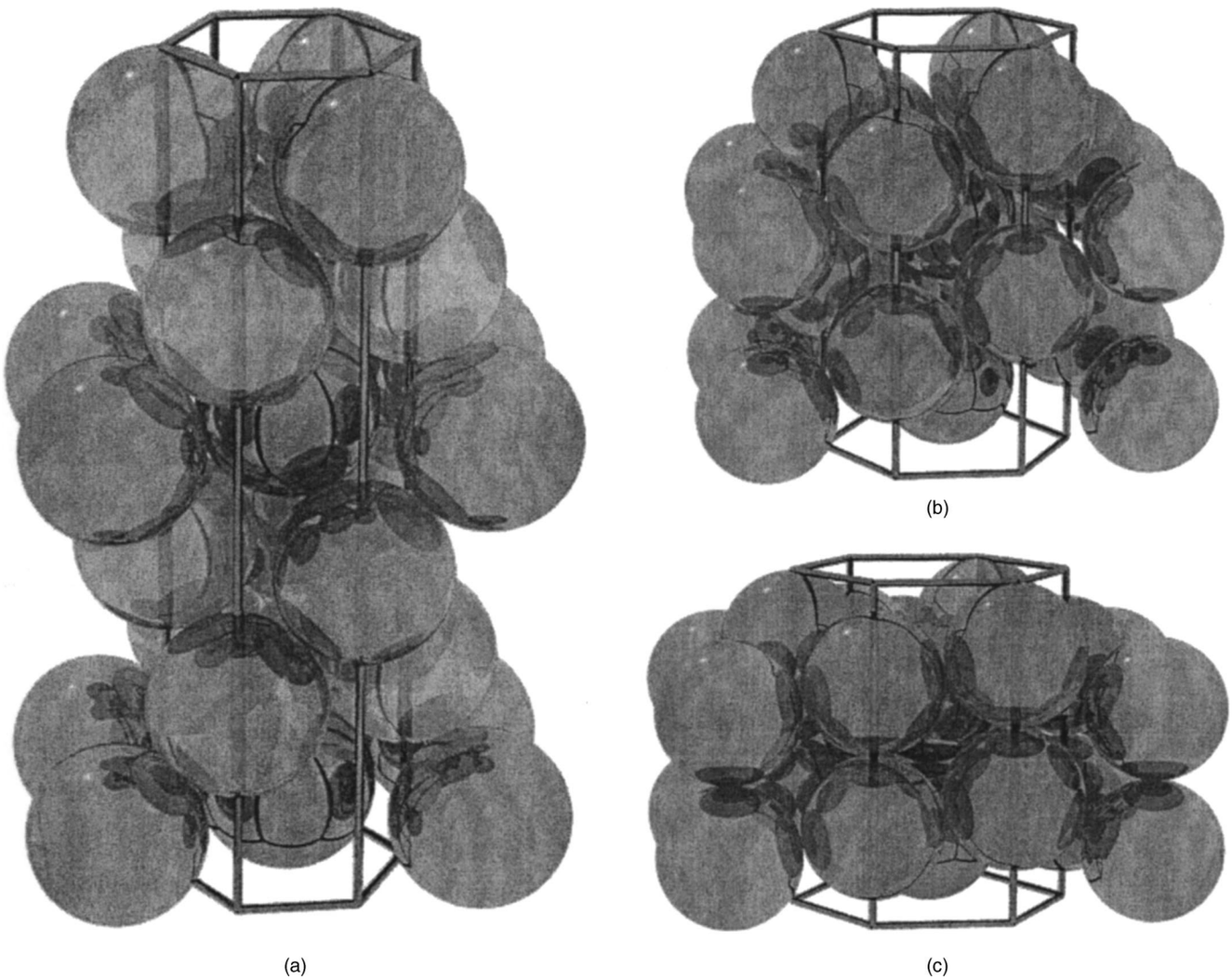

Figure 5. Six-layered unit cell with separation factor f = (a) 2.3, (b) 3.15, and (c) 3.4.

$$T = 2 + (n - 1)IH \quad [10]$$

where IH is the differential height increment, determined from geometry to be

$$IH = \sqrt{4 - \frac{f^2}{3}} \quad [11]$$

for $n > 1$ and 1 radius unit (repeated twice) for $n = 1$. The thickness of an overlap band in tightly packed cases is readily seen in Fig. 4 to be the thickness of a single sphere, less the differential height increment, or $2 - IH$. The number of slices in the asymmetric half of the overlap band is rounded up to the nearest integer using,[12] where $Ceiling[x]$ is defined as the smallest integer $\geqslant x$

$$n_{OB} = Ceiling\left[\frac{N}{2}\frac{2 - dH}{T}\right] \quad [12]$$

Figure 4 likewise indicates that the interlayer gap thickness is that of one sphere less two full overlap bands $2 \times IH - 2$. When there are three or more layers, the number of slices in this region is then

$$n_G = Ceiling\left[\frac{N}{2}\frac{2IH - 2}{T}\right] \quad [13]$$

and zero when there are two or fewer layers. The remaining slices are allocated to the incremental height region

$$n_{IH} = N/2 - (n - 1)n_{OB} - (n - 2)n_G \quad [14]$$

Equations 12-14 are valid for $f \leqslant 3$ but can be generalized to the other situations. Individual segment thicknesses Δ are then calculated based on these new integer values and used to calculate slice resistances based upon particle resistivities and the particle or solution area within the segment. The area A of the kth slice (of radius r) of a sphere (with radius R) is calculated as

$$r^2 = R^2 - [R - k(\Delta R)]^2$$

$$r^2 = k\Delta R(2R - k\Delta R)$$

$$A = \pi k\Delta(2 - k\Delta) \quad [15]$$

where Δ and A are in dimensionless radius units. This formula is valid in the end IH region where $0 \leqslant k\Delta \leqslant 2$ and can be generalized to other regions with appropriate slice height offsets. Electrolyte solution area is found by subtracting particle area from that of the unit cell. The interfacial surface area of a slice through a sphere is dependent only on its thickness and does not vary with its location within a sphere. Interfacial area values were weighted appropriately

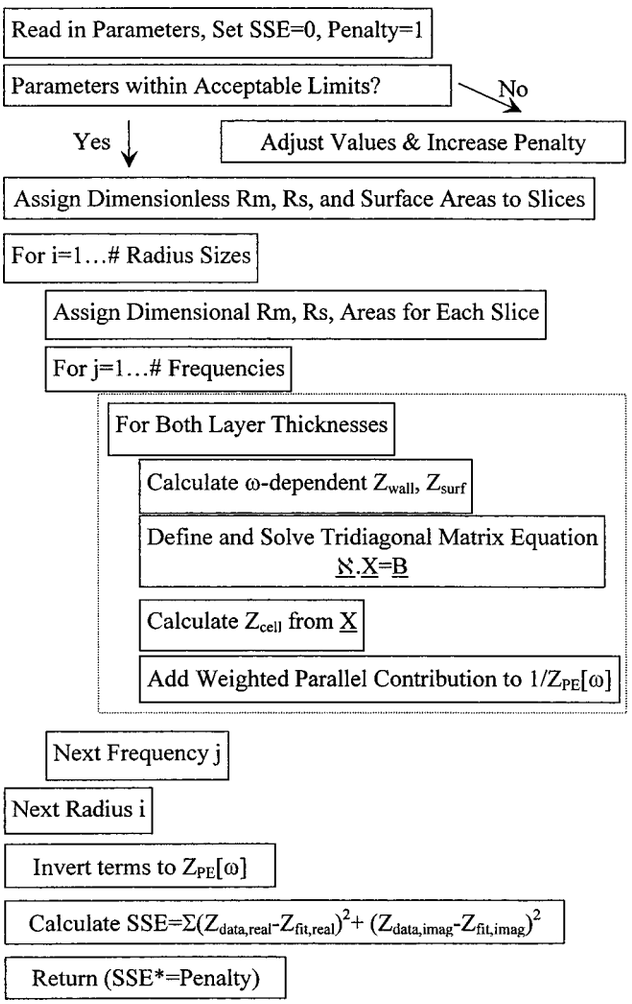

Figure 6. Flowchart of model implementation.

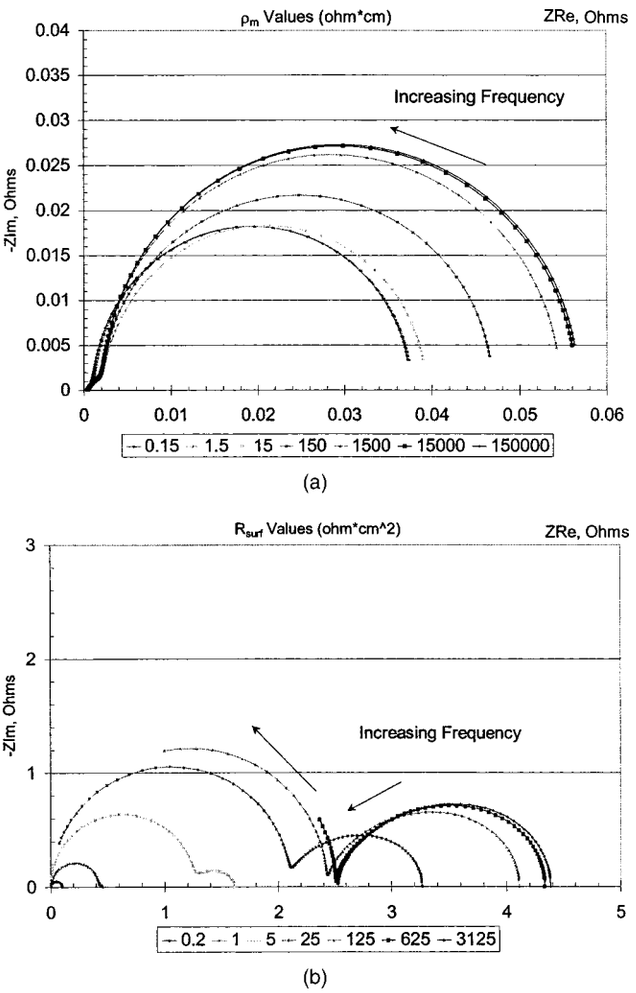

Figure 7. Dependence of impedance spectra on (a) ρ_m and (b) R_{surf}.

in slices containing multiple spheres. Our model used 100 slices per sphere, which seemed sufficient for convergence of our surfaces. A flowchart of the model's implementation is shown in Fig. 6.

Analysis of Parameters

Particle resistivity was the primary value sought from analysis of the experimental data, so it was essential to understand its influence on impedance spectra. A series of simulations were performed with default parameter values of: $\rho_m = 15{,}000\ \Omega$ cm; $RC_w = 0.15$ s; $RC_{surf} = 0.5$ ms; $R_{ext} = 0$; $R_w = 0.25\ \Omega\ cm^2$; $R_{surf} = 40\ \Omega\ cm^2$; $n_{avg} = 1.5$; and $f = 2.5$. Particle resistivity ρ_m was varied between 0.15 and 150,000 Ω cm, with representative traces shown in Fig. 7a. When the particle resistivity is very low (relative to other components), the impedance spectrum is semicircular, with only weak dependence upon the exact resistivity value. This suggests that for low ρ_m the interior is highly conductive relative to other components. As the resistivity increases, the frequency response deforms, passing through an initial plateau (sometimes only partially formed and seen as a pronounced difference in slope) before reaching a second arc, which progressively extends with increasing ρ_m. At high values of ρ_m, the arcs again converge in a near semicircle (with the initial deformation) as current now passes almost exclusively through the solution. Physically, this suggests a transition from conductance primarily through the particle to a shared particle/solution pathway until the solution itself dominates.

The specific resistance of the surface R_{surf} was varied between 0.2 and 3125 $\Omega\ cm^2$. Both magnitudes and shapes of the spectra varied dramatically with low values of resistance but were invariant for values large enough to restrict entry of current through the surface pathway. Figure 7b indicates that at very small resistances there was only a single arc of small magnitude indicating current passing primarily through this low-resistance pathway. As the surface resistance increased so did the magnitude of this primary arc; moreover, a second arc began to manifest itself, indicating a second pathway (through the particles) for the current to travel. At very high resistances, curve magnitudes again became nearly invariant, as other factors dominated; the frequency response, however, was increasingly constrained to the low-frequency regions of the spectrum. This is likely a result of the choice of testing parameters. As R_{surf} increases at constant RC_{surf}, the capacitance diminishes accordingly and saturates at lower frequencies.

As the particle wall's specific resistance was varied between 0.25 and 250,000 $\Omega\ cm^2$ the magnitudes of the spectra again increased. In regions where two distinct arcs are present corresponding to two viable current pathways (as in Fig. 8), increasing R_w increases the size of the low-frequency semicircle until that feature alone dominates. The size of this semicircle likely indicates the extent to which current flows through the solution-surface pathway, avoiding the support and catalyst. Relative improvement in the size of the first arc

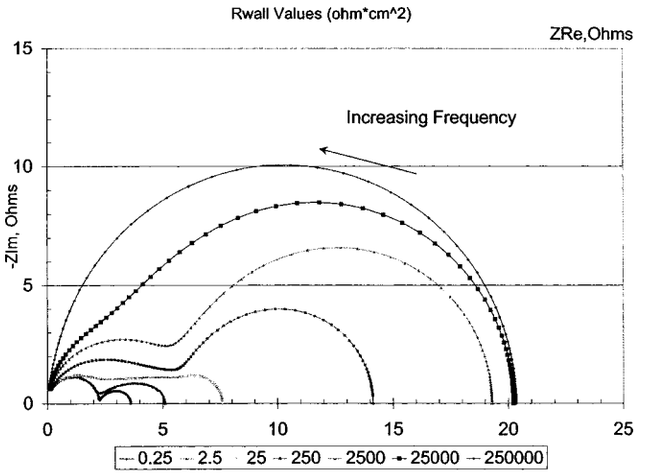

Figure 8. Dependence of impedance spectra on R_{wall}.

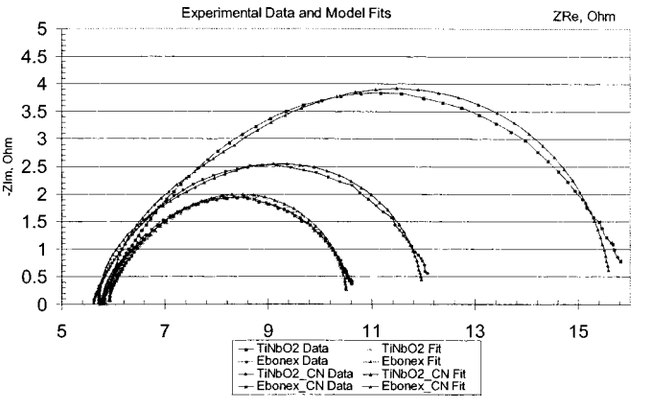

Figure 9. Nyquist plots of experimental and fit impedances.

in experimental samples should then correlate to more efficient catalyst utilization.

In most cases, the two resistance-capacitance (RC) time constants were not observed to have any influence on the shape of the impedance curves other than the predictable effect of shifting the frequency response along the path of the previous loci. Nevertheless, in some cases where the spectra possessed pronounced double humps, these parameters appeared to have some influence upon the location of the transition and the sharpness of its inflection. These effects defy ready generalization, but any simulations performed in such regions should pay particular care to the choice of these parameters.

Discussion of Experimental Fits

Model parameters were fit to experimental data based on a minimization of sum-squared error (SSE)

$$SSE = \sum_{\text{all frequencies}} [(Z_{\text{data,re}} - Z_{\text{fit,re}})^2 + (Z_{\text{data,im}} - Z_{\text{fit,im}})^2] \quad [16]$$

using a direction set method after manually determining plausible initial guesses. Minimizations of each set were performed from several starting points. Poor guesses led to high SSE local minima with obviously incorrect fits, but all optima with SSE values less than 2.0 possessed approximately the same solution values. The lowest minima are reported along with error estimates calculated at the 95% confidence level using the relationship

$$SSE_{95\%}[\mathbf{S}] = SSE[\hat{\mathbf{S}}]\left(1 + \frac{P}{N_{\text{set}} - P} F[P, N_{\text{set}} - P]\right) \quad [17]$$

N_{set} represents the number of data points in the spectrum data set; P is the number of adjustable parameters (eight); $F[P,\ N_{\text{set}} - P]$ is the value of the statistical F distribution at the indicated number of degrees of freedom and confidence levels; $\hat{\mathbf{S}}$ is the optimal parameter set; and $\mathbf{S}$ is the optimal solution set with one parameter changed to make the equality true. Nyquist and Bode plots of the original data sets[10] and fits can be seen in Fig. 9 and 10. Best-fit values for the four supports are found in Tables I-IV.

Although resistance terms were calculated as resistivities and specific resistances, it is also instructive to compare the magnitudes of each component's actual contribution to resistance. Therefore, for each data set resistances were calculated for the particle material, wall, surface, and solution based on the optimal parameter values and surface geometry (see Table 1 in Ref. 10). These results challenge our initial assumptions regarding the use of porous electrodes in catalysis. The three parameters that changed most between sets were the material conductivity, the time constant of the wall interface, and the specific resistance of the particle-surface interface. Resistivities could vary between 0.8 and 4 Ω cm for the as-

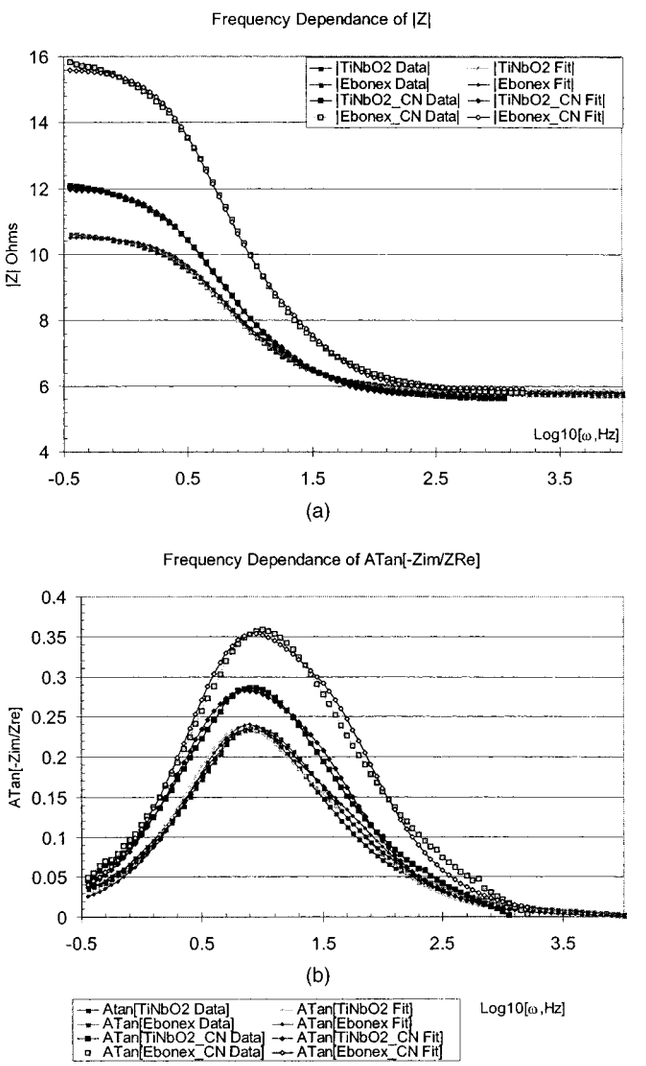

Figure 10. Bode plot of experimental and fit impedance magnitudes: (a) and (b).

Table I. $Pt_4Ru_4Ir/Ti_{0.9}Nb_{0.1}O_2$, SSE 0.371.

Parameter	Best fit value	Low 95% confidence	High 95% confidence
ρ_m, Ω cm	5.1×10^3	4.3×10^3	6.2×10^3
RC_{wall}, s	1.6×10^2	1.5×10^2	1.7×10^2
RC_{surf}, s	0.088	0.084	0.093
R_{ext}, Ω cm^2	9.18	9.14	9.23
R_{wall}, Ω cm^2	5.9×10^4	5.4×10^4	6.4×10^4
R_{surf}, Ω cm^2	7.3	7.2	7.4
n_{avg}	1.648	1.641	1.654
f	2.339	2.335	2.344

synthesized support materials[14] to roughly 1 MΩ cm for the completely oxidized forms, and it was expected that the supports conditioned for only 30 min would possess values very near those of the as-synthesized materials. In contrast, the calculated resistivities of both Pt_4Ru_4Ir/Ebonex and $Pt_4Ru_4Ir/Ti_{0.9}Nb_{0.1}O_2$ of several thousand ohms per centimeter indicate partially oxidized starting states. Resistance can be a complicated function of the oxidation state, but if resistance increases linearly or supralinearly with oxidation, this implies an oxidation percentage of less than 1%, which is physically plausible. It was also hypothesized that conditioning would increase the particle resistivities dramatically due to increased oxidation. Resistivities did increase by up to a factor of three, but this was much less than expected. If the particle surfaces were previously oxidized, that may have slowed subsequent oxidation of the interior during the conditioning phase. Moreover, this change seems unlikely to influence the overall electrode response, as the wall impedance in series with the interior is considerably larger.

Table II. $Pt_4Ru_4Ir/Ti_{0.9}Nb_{0.1}O_2$ conditioned for 7 h, SSE 0.590.

Parameter	Best fit value	Low 95% confidence	High 95% confidence
ρ_m, Ω cm	1.4×10^4	1.0×10^4	1.6×10^4
RC_{wall}, s	1.4×10^2	1.2×10^2	1.5×10^2
RC_{surf}, s	0.105	0.103	0.115
R_{ext}, Ω cm^2	9.5	9.4	9.6
R_{wall}, Ω cm^2	6.0×10^4	5.4×10^4	6.6×10^4
R_{surf}, Ω cm^2	10.5	10.3	10.6
n_{avg}	1.40	1.39	1.41
f	2.225	2.219	2.232

Table III. Pt_4Ru_4Ir/Ebonex, SSE 0.368.

Parameter	Best fit value	Low 95% confidence	High 95% confidence
ρ_m, Ω cm	5.7×10^3	4.8×10^3	6.8×10^3
RC_{wall}, s	145.0	136.0	158.0
RC_{surf}, s	0.077	0.073	0.081
R_{ext}, Ω cm^2	9.08	9.04	9.13
R_{wall}, Ω cm^2	5.8×10^4	5.3×10^4	6.2×10^4
R_{surf}, Ω cm^2	7.46	7.38	7.56
n_{avg}	1.487	1.482	1.494
f	2.225	2.220	2.229

Table IV. Pt_4Ru_4Ir/Ebonex conditioned for 7 h, SSE 1.39.

Parameter	Best fit value	Low 95% confidence	High 95% confidence
ρ_m, Ω cm	1.7×10^4	1.4×10^4	1.9×10^4
RC_{wall}, s	85.0	78.0	92.0
RC_{surf}, s	0.086	0.082	0.091
R_{ext}, Ω cm^2	10.4	10.3	10.5
R_{wall}, Ω cm^2	5.8×10^4	5.4×10^4	6.3×10^4
R_{surf}, Ω cm^2	17.1	16.8	17.3
n_{avg}	1.36	1.35	1.37
f	2.25	2.24	2.26

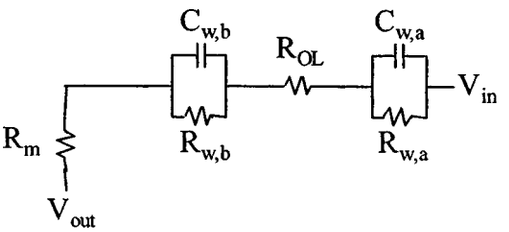

Figure 11. Proposed equivalent circuit for current flowing through a resistive oxide shell.

The RC time constant of the wall also seemed to decrease during conditioning, but it is unclear whether this holds significance in electrode design. It must be noted that the two electrodes conditioned for only 30 min had virtually identical responses yet possessed time constants differing by 15 s. Untreated Ebonex and treated $Ti_{0.9}Nb_{0.1}O_2$ were quite different but had a smaller difference in time constants on both absolute (5 s) and relative scales. As the wall specific resistivities remained virtually constant in all samples, the decreased time constants are due almost exclusively to diminished wall capacitances.

Both characteristics of the wall might be explained if the conditioning process creates an ever-thickening partially oxidized shell around a more conductive particle interior. In this more complicated model, shown in Fig. 11, net current flow would still pass through a resistor R_{wa} and capacitor C_{wa} in parallel at the particle-solution interface. They would then pass through the highly resistive oxide layer R_{OL} (which is physically likely to have a composition gradient rather than uniformity) and then pass through another resistor-capacitor pair R_{wb}/C_{wb}, before traversing the particle's interior resistance R_m and continuing to the next segment. Mathematically, the net impedance of this pathway at frequency ω would be

$$Z = R_{OL} + R_m + \left(\frac{R_{wa}}{1 + (\omega R_{wa}C_{wa})^2} + \frac{R_{wb}}{1 + (\omega R_{wb}C_{wb})^2}\right) - j\left(\frac{\omega R_{wa}^2 C_{wa}}{1 + (\omega R_{wa}C_{wa})^2} + \frac{\omega R_{wb}C_{wb}}{1 + (\omega R_{wb}C_{wb})^2}\right) \quad [18]$$

in contrast to the model studied where R_{wb} and R_{OL} were zero. If the thickness of the oxide layer increases, the frequency-independent R_{OL} would increase and be incorporated into the R_m term (as ρ_m), producing the observed increase upon conditioning. Once the current had penetrated the particle interior, this value would continue to have an apparent increase due to the more constricted cross-sectional area of the conductive bulk. Physically, R_{wa} and R_{wb} and their composite R_w might be expected to remain unchanged upon oxidation as the interfaces remain the same and only the oxide thickness changes. Analysis of the capacitance is more complicated, but in the model of a single equivalent capacitor with one plate on either side of the oxide layer, plate separation can clearly be considered to have increased after conditioning. As parallel-plate capacitance is inversely proportional to this larger separation (or, alternatively, concentric sphere capacitance is proportional to the now-diminished radius), the net capacitance lessens, as does the RC time constant. Alternatively, one may view the capacitance change as a reflection of the entire system. For reasons described later, conditioning increased the current entering the upper regions of the spherical supports, possibly influencing the nature of the electrical double layer in those regions. Finally, note that in Fig. 9 most of the fit error comes from the low-frequency region of the spectrum and this is the region where terms containing the time constant become largest; thus, the observed trend may to some extent be an artifact of fitting errors.

In contrast with expectations, the parameter that seemed to hold the most influence over the impedance spectra was the specific resistance of the particle-carbon paper surface interface. Comparison

with the minima in the impedance curves yielded a correlation coefficient of 0.9999. In light of the other results, this seems physically reasonable. The impedance of the particle walls is so large that it forces most current to enter the spheres as close to the base as possible and the limiting resistance becomes the surface impedance. This observation suggests utilization of any electrocatalyst on an oxide support is very low if R_{wall} is high. The internal resistance of the particles is an order of magnitude less than that of the surface and more than four orders of magnitude less than that of the walls. At present, it seems catalyst utilization can be improved by continuing to increase the surface impedance, forcing more current through the spheres and the catalysts coating their surface. This might be acceptable in some applications but would decrease the voltage obtained if used in fuel cells. The same effect might be achieved by using a less conductive electrolyte solution, but at the cost of a higher external resistance. Vast improvements in current distribution, however, could be obtained if the wall impedance were diminished until it was comparable to or less than the other resistive components. Even then, the resistance due to the particles after 30 min conditioning exceeds that of the surrounding sulfuric acid electrolyte. If surface impedance can be maintained without conditioning, that may improve catalyst utilization. Electrode improvement may also be achieved by designing electrode construction to minimize wasteful multilayers and to encourage close packing. In limited applications not requiring fine particles of catalytically active composites, inefficiency might be reduced by plating the catalyst from a solution onto the supports, thus matching metal deposition with current distribution.

These observations also suggest possible improvements in the mathematical model. It was initially assumed that current only passed into the carbon paper support where it was in contact with the semiconducting spheres. In light of the high particle resistances and the limiting effect of the surface impedance, this assumption seems suspect. Although there is danger in including too many parameters in mathematical models of physical systems, the addition of a solution to surface capacitance and a parallel resistance not confined to the contact point may be justified.

Conclusions

Fuel cell and bifunctional electrodes often make use of finely divided noble metals or noble metal oxides on conductive supports, which may then be treated to enhance thermal stability. Unfortunately, the influence of such processes on the electrochemical properties of the electrodes is poorly understood. A physically reasonable transmission line model has shown that four oxidatively conditioned electrodes suffer from poor catalyst utilization because of unchangingly large impedances at the solution/support interface, most likely due to oxidation of the support and/or the supported catalysts. Increased semiconductor/carbon paper impedances might improve utilization slightly, but at the cost of higher overall resistances. Conditioning also decreases the capacitance of the support particles, possibly by a thickening of an oxide shell around a semiconducting interior.

This model suggests a number of approaches to improving electrode design. Porous electrodes are typically made with conductive materials, but these may degrade under high temperatures or anodic potential conditions. This problem is of less concern for fuel-cell anode catalysts, which are operated at relatively low potentials, but it can be quite significant for fuel-cell cathodes or for electrolyzer catalysts. In the case of oxide supports, vast gains in utilization could be achieved if a technique can be found to give the support particle resistivities comparable to those of the electrolyte solution. The results also suggest determining the properties of unconditioned electrodes as a first step in striking a balance between stability and utilization. Conditioned electrodes might also be exposed to reducing conditions to assess the reversibility of the changes. In short, this model provides a general tool for determining the detailed electrochemical properties of porous electrodes, enables the testing of some mechanistic hypotheses (the recent postulate that catalyst additives act by improving electrical contact between catalyst surfaces and the electrolyte phase,[15] for example), and provides a method to monitor the success of optimization efforts (such as attempts to inhibit the formation of insulating anodic films by alloying Pt with Fe, Co, or Cr).[16,17] The understanding gained from these studies can then supplement the primary search for better catalysts by isolating the effects of the electrode and suggesting means for overall improvement.

Acknowledgments

This work was supported by a grant from the Army Research Laboratory, Collaborative Technology Alliance in Power and Energy, and by the U.S. Department of Energy through grant DE-FG02-01ER 15238.

The Pennsylvania State University assisted in meeting the publication costs of this article.

List of Symbols

$\underline{\underline{A}}$	Matrix of Kirchoff's voltage law current coefficients, Ω
$\mathbf{B}$	vector of impedances in Kirchoff's voltage law equations, Ω
$\mathbf{X}$	vector of relative currents in Kirchoff's voltage law equations
A	dimensionless cross-sectional area of a slice of a unit sphere
D	diameter of a semiconducting sphere, μm
f	dimensionless sphere separation factor, $X = fr$, $2 \leqslant f < 2\sqrt{3}$
G	dimensionless height of the gap region, radius units
IH	dimensionless height of the incremental height region, radius units
i_k	current traversing the kth Kirchhoff voltage loop, A
i_0	current passing from voltage source through particle to ground, A
j	unit length imaginary component $\sqrt{-1}$
k	iterator
m	mass of semiconducting material deposited, g
n	number of layers of spheres in the region under examination
N	total number of slices in one half of the unit cell
N_{part}	total number of particles coating surface
N_{set}	number of data points in each data set
n_{avg}	average number of layers coating electrode surface
n_{base}	smaller number of layers assumed to cover the electrode surface
n_{frac}	fraction of the electrode surface covered by the $n_{base} + 1$ layers
n_G	number of slices in the asymmetric half of the gap region
n_{IH}	number of slices in the asymmetric IH region
n_{OB}	number of slices in the asymmetric half of the OB region
OB	dimensionless height of the OB region, radius units
P	number of adjustable parameters
$p[D]$	lognormal probability density function
r	radius of a semiconducting sphere, μm
RC_{surf}	time constant of the sphere-electrode surface interface, s
RC_w	time constant of the sphere wall-solution interface, s
R_{ext}	external resistance (used in Kirchoff equations), Ω, or specific external resistance (used in optimization model), Ω cm^2
R_m	resistance due to semiconducting material, Ω
R_s	resistance due to electrolyte solution, Ω
R_{surf}	specific surface resistance, Ω cm^2
R_w	specific resistance of the sphere wall-solution interface, Ω cm^2
$\mathbf{S}$	vector containing adjustable model parameters
$\hat{\mathbf{S}}$	vector containing the optimal solution set parameters
SSE	sum squared error used to optimize fits
T	dimensionless layer thickness as a multiple of sphere radius
V	applied voltage, V
X	separation distance between nearest-neighbor spheres on electrode surface, cm
$\mathbf{X}$	vector of relative currents in Kirchoff's voltage law equations
Z	impedance at an interface, Ω
Z_{cell}	impedance in one unit cell, Ω
Z_k	impedance of the kth slice, Ω
Z_{PE}	impedance of the entire porous electrode, Ω
Z_{surf}	impedance of the electrode surface, Ω
μ	mean of lognormal distribution
ρ	density of semiconducting material, g/cm^3
ρ_m	resistivity of the spherical semiconducting material, Ω cm
ρ_s	resistivity of the electrolyte solution, Ω cm
σ	standard deviation of lognormal distribution
ω	angular frequency of ac current, rad/s

References

1. I. R. Burrows, D. A. Denton, and J. A. Harrison, *Electrochim. Acta*, **23**, 493 (1978).
2. S. D. Bhakta, D. D. Macdonald, B. G. Pound, and M. Urquidi-Macdonald, *J. Electrochem. Soc.*, **138**, 1353 (1991).
3. D. T. Sheih and B. J. Hwang, *Electrochim. Acta*, **15**, 2239 (1993).
4. J. Fleig and J. Maier, *J. Electroceram.*, **1**, 73 (1997).

5. D. D. Macdonald, M. Urquidi-Macdonald, S. D. Bhakta, and B. G. Pound, *J. Electrochem. Soc.*, **138**, 1359 (1991).
6. J. R. Park and D. D. Macdonald, *Corros. Sci.*, **23**, 295 (1983).
7. H. Kaiser, K. D. Beccu, and M. A. Gutjahr, *Electrochim. Acta*, **21**, 539 (1976).
8. G. Chen, S. R. Bare, and T. E. Mallouk, *J. Electrochem. Soc.*, In press.
9. G. Chen, S. Sarangapani, and T. E. Mallouk, *Catal. Today*, **67**, 341 (2001).
10. G. Chen, C. C. Waraksa, T. E. Mallouk, and D. D. Macdonald, *J. Electrochem. Soc.*, **150**, E423 (2003).
11. D. D. Macdonald, in *Techniques for Characterization of Electrodes and Electrochemical Processes*, R. Varma and J. R. Selman, Editors, pp 515–580, Wiley, New York (1991).
12. W. H. Press, S. A. Teukolsky, W. T. Vetterling, and B. P. Flannery, *Numerical Recipes in C: The Art of Scientific Computing*, 2nd ed., Cambridge, New York (1995).
13. *Handbook of Electrolyte Solutions, Part A*, V. M. M. Lobo, Editor, Elsevier Science Publishers, B.V., New York (1989).
14. E. E. Farndon and D. Pletcher, *Electrochim. Acta*, **42**, 1281 (1997).
15. J. W. Long, R. M. Stroud, K. E. Swider-Lyons, and D. R. Rolison, *J. Phys. Chem. B*, **104**, 9772 (2000).
16. T. Toda, H. Igarashi, H. Uchida, and M. Watanabe, *J. Electrochem. Soc.*, **146**, 3750 (1999).
17. S. Gamburzev, O. Velev, S. Srinivasan, A. Appleby, F. Lucaz, and D. Wheeler, in *Electrode Materials and Processes for Energy Conversion and Storage IV*, S. Srinivasan, J. McBreen, A. C. Khandkar, and B. V. Tilak, Editors, PV 97-13, p. 78, The Electrochemical Society Proceedings Series, Pennington, NJ (1997).